CHEMISTRY

Discovery of BODIPY J-aggregates with absorption maxima beyond 1200 nm for biophotonics

Xiaoqing Wang[1]†, Zhiyong Jiang[2,3]†, Zhaolun Liang[2], Tianzhu Wang[2], Yuncong Chen[3], Zhipeng Liu[1,2,4]*

Organic dyes with absorption maxima in the second near-infrared window (NIR-II; 1000 to 1700 nm) are of great interest in biophotonics. However, because of the lack of appropriate molecular scaffolds, current research in this field is limited to cyanine dyes, and developing NIR-II–absorbing organic dyes for biophotonics remains an immense challenge. Here, we rationally designed an ethenylene-bridged BODIPY scaffold featuring excellent J-aggregation capabilities and revealed that the bridging ethylene unit is crucial for intermolecular J-coupling regulation. By integrating the electron-donating groups into the scaffold, we obtained a BODIPY dye, BisBDP2, with a J-aggregate absorption maximum of around 1300 nm. BisBDP2 J-aggregates show excellent photothermal performance, including intense photoacoustic response, and a high photothermal conversion efficiency value of 63%. In vivo results demonstrate the potential of J-aggregates for photoacoustic imaging and photothermal ablation of deep-seated tumors. This study will speed up the exploration of NIR-II–absorbing J-aggregates for future biophotonic applications.

INTRODUCTION

Organic dyes that absorb near-infrared (NIR) light are of immense interest in biophotonics because of their outstanding biocompatibility and biodegradability (*1*–*2*). Among these dyes, those capable of absorbing in the second NIR window (NIR-II; 1000 to 1700 nm) are more attractive because of their low phototoxicity and deep-tissue penetration (*3*–*7*). However, the design of NIR-II–absorbing organic dyes for biophotonics is mainly limited to cyanine dyes (*6*–*14*), and their development remains an immense challenge.

Attempts to achieve NIR-II–absorbing organic dyes have mainly focused on molecular engineering approaches including expanding the π-conjugation structure and strengthening the donor-acceptor conjugation. Unfortunately, only a few successful paradigms have been validated because of the lack of suitable scaffolds (*3*–*6*, *12*–*23*). J-aggregation, which is characterized by a notable bathochromic-shifted absorption band after J-coupling in the excited state, provides an immense opportunity to convert the NIR-I absorption of organic dyes to the NIR-II window (*24*, *25*). Pioneer examples of NIR-II–absorbing J-aggregates based on cyanine and squaraine have recently been realized. Chen *et al.* (*26*) have prepared stable J-aggregates of IR-140 with absorption maximum (λ_{abs}) at 1040 nm by aggregating IR-140 dyes in hollow mesoporous silica nanoparticles (NPs). Sun *et al.* (*27*) reported J-aggregates of FD-1080 dye that show λ_{abs} at 1360 nm and emission maximum (λ_{em}) at 1370 nm for NIR-II fluorescence imaging (*7*). Shen *et al.* (*28*) have reported that the NIR-II absorption of squaraine can be efficiently achieved by using a double J-coupling strategy. Although the preceding elegant examples demonstrate the feasibility of J-aggregation for the development of NIR-II–absorbing organic dyes, the rational design and stabilization of J-aggregates based on small organic dyes in complex settings require further exploration.

As one of the most famous classical dyes, BODIPY (4,4-difluoro-4-bora-3a,4a-diazas-indacene) dyes (*29*) are recently recognized as promising J-aggregation scaffolds in parallel with cyanine, squaraine, perylenediimide, and chlorophyll dyes (*30*–*34*). Numbers of NIR-I–absorbing BODIPY J-aggregates were developed and demonstrated the application potential in biophotonics (*35*–*42*). For example, Li and colleagues (*40*, *42*) prepared BODIPY J-aggregates for in vivo fluorescence imaging and photothermal therapy (PTT) via the halogen bonding–triggered J-aggregation of halogenated BODIPY monomer. Guo *et al.* (*39*) reported the phenanthrene-[*b*]–fused BODIPY J-aggregates that show λ_{abs} at 840 nm for PTT applications under 808-nm laser irradiation. Chen *et al.* (*35*) developed aza-BODIPY J-aggregates with in situ morphology transformation ability for PTT application. All these achievements motivated us to explore NIR-II–absorbing BODIPY J-aggregates. Here, we present an ethenylene-bridged BODIPY dye (**BisBDP1**) as a scaffold for constructing NIR-II–absorbing BODIPY J-aggregates. **BisBDP1** itself exhibited excellent J-aggregation behavior. Upon integration of tetrahydroquinoxaline (THQ) units into the scaffold, the resulting BODIPY dimer (**BisBDP2**) not only bathochromic-shifted its monomeric absorption maximum (λ_{abs}) around 1100 nm but also displayed J-aggregation behavior with λ_{abs} around 1300 nm. Moreover, the **BisBDP2** J-aggregates were also demonstrated to be applicable to photoacoustic (PA) imaging–guided PTT (Fig. 1).

RESULTS

Molecular design

Cyanine dyes with ethylene bridges typically exhibit excellent J-aggregation properties (*24*, *43*, *44*). To determine whether it could also be effective with BODIPY dyes, we designed an ethenylene-bridged BODIPY dye (**BisBDP1**). We selected the BODIPY dye with trifluoromethyl at the meso-position as the chromophore (CF_3-BODIPY) to construct **BisBDP1**. When compared to classical BODIPY dyes with methyl and phenyl groups at the meso-position,

[1]College of Science, Nanjing Forestry University, Nanjing 210037, China. [2]College of Materials Science and Engineering, Nanjing Forestry University, Nanjing 210037, China. [3]State Key Laboratory of Coordination Chemistry, School of Chemistry and Chemical Engineering, Nanjing University, Nanjing 210093, China. [4]Co-Innovation Center of Efficient Processing and Utilization of Forest Resources, Nanjing Forestry University, Nanjing 210037, China.
*Corresponding author. Email: zpliu@njfu.edu.cn
†These authors contributed equally to this work.

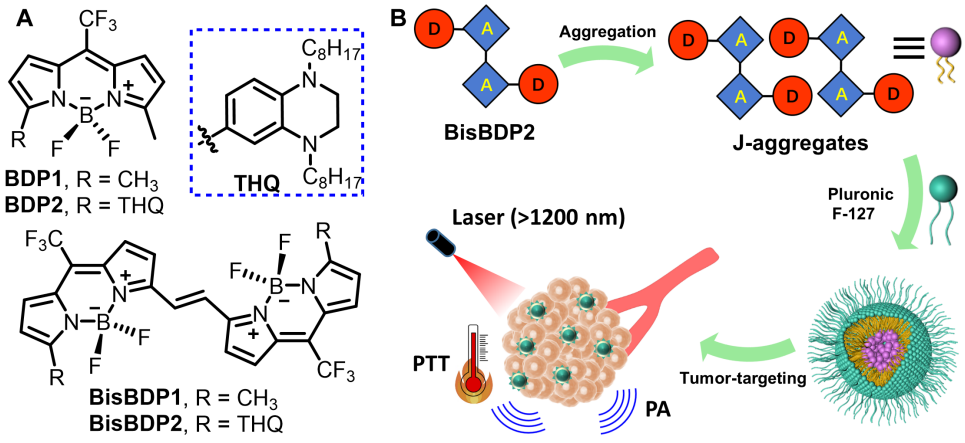

Fig. 1. Molecular structures and working principle. (**A**) Chemical structures of **BDP1**, **BDP2**, **BisBDP1**, and **BisBDP2**. (**B**) Schematic illustration of the PA imaging–guided PTT in the NIR-II window using **BisBDP2** J-aggregates.

CF_3-BODIPY dyes typically show bathochromic-shifted λ_{abs} because of the excellent electron-withdrawing ability of the CF_3 group (*32*). This would be helpful for bathochromic shifting the λ_{abs} of **BisBDP1**. On the other hand, **BisBDP1** is highly expected to bathochromic-shift the λ_{abs} to the NIR region because many ethenylene-bridged BODIPY dyes exhibit 100- to 200-nm bathochromic-shifted λ_{abs} in comparison to their monomer (*19*, *45*, *46*). Taking the advantage of highly electron-accepting nature of CF_3-BODIPY, we further developed donor-accepter-π-accepter-donor (D-A-π-A-D)–structured BODIPY dye (**BisBDP2**) by integrating two THQ units with strong electron-donating ability into the **BisBDP1** scaffold to achieve the further λ_{abs} bathochromic shift (*20*). Moreover, the "zig-zag" type D-A-π-A-D of **BisBDP2** would help generate intermolecular J-coupling in the aggregation state; thus, the bathochromic-shift absorption of the J-aggregates to the NIR-II window is highly expected.

Synthesis and characterization

The synthesis of **BisBDP1** and **BisBDP2**, as well as their corresponding monomers **BDP1** and **BDP2**, is outlined in fig. S1. The molecular and packing structures of **BisBDP1** were characterized by single-crystal x-ray crystallography (Fig. 2A and table S1). In the molecular structure of **BisBDP1**, two ethenylene-bridged indacene planes are well planned for each other. Notably, **BisBDP1** are packed in a "head-to-tail" mode with a slipping angle of 27°, and the distance between each monomer is around 3.68 Å (Fig. 2B and fig. S2). Each monomer was connected via the π···π (3.68 Å) and C···F (2.99 Å) intermolecular interactions (fig. S3). The interaction between the two indacene planes and the strong C…F interactions play key roles in the formation of J-type molecular structure.

Photophysical properties in the diluted solution

We investigated the photophysical properties of **BDP1** and **BDP2** and **BisBDP1** and **BisPDP2** in dichloromethane solution (table S2). **BDP2** showed its λ_{abs} at 735 nm (ε_{max} = 41000 M^{-1} cm^{-1}), which is bathochromic-shifted 191 nm comparing to the meso-CF_3-BODIPY core (**BDP1**, λ_{abs} = 544 nm; fig. S4) (*32*). The "push-pull" effect from the THQ unit to the BODIPY core should be responsible for this large bathochromic-shifted absorption. Compared with **BDP1**, the λ_{abs} of **BisBDP1** (λ_{abs} = 760 nm, ε_{max} = 129,000 M^{-1} cm^{-1}) is bathochromic-shifted by 216 nm, and this trend is comparable with those reported ethenylene-bridged BODIPY dyes (*19*, *45*, *46*). Notably, **BisBDP2** showed its λ_{abs} at 1112 nm (ε_{max} = 78000 M^{-1} cm^{-1}), which is 377 and 352 nm bathochromic-shifted compared to **BDP2** and **BisBDP1** (Fig. 2C). According to the above results, the synergy of extended π-conjugation and push-pull effects is responsible for extraordinary large bathochromic shifts. Note that **BisBDP2** is the first known small BODIPY dye with monomeric λ_{abs} beyond 1100 nm, and the design strategy for **BisBDP2** is expected to offer opportunities for the development of NIR-II–absorbing BODIPY dyes.

Consistent with the results obtained in the absorption spectra, **BDP2** showed a broad emission band with an emission maximum (λ_{em}) around 995 nm and a quantum yield (Φ_f) of 1.5% (fig. S5). Compared to the intense green emission of **BDP1** (λ_{em} = 547 nm, Φ_f = 92%), the large bathochromic-shifted λ_{em} (448 nm) and decreased quantum yield further indicated the stronger intramolecular charge transfer (CT) intrinsic character of **BDP2** than **BDP1** (*47*). **BisBDP1** displayed one sharp peak and two relative broad peaks with λ_{em} at 788, 870, and 975 nm, respectively, which may be ascribed to the local and CT emissions, respectively. Because of the extended conjugation and push-pull effect, **BisBDP2** further bathochromic-shifted its emission to the NIR-II window, with the λ_{em} around 1314 nm. These results further proved the importance of the synergy of the push-pull and conjugation effect on the bathochromic shift of the emission wavelength. However, the Φ_f of **BisBDP1** and **BisBDP2** is too low to be determined, indicating the strong fluorescence quenching caused by the push-pull effect (*20*, *21*).

Theoretical calculations

The photophysical properties of the monomers and dimers can be well rationalized by theoretical calculations. The calculation results demonstrated that the first absorption bands of **BDP1**, **BDP2**, **BisBDP1**, and **BisBDP2** are contributed mainly by the transition from the highest occupied molecular orbital (HOMO) to the lowest unoccupied molecular orbital (LUMO), and the transition energies are in good agreement with the experiment results. As shown in fig. S6, the electron density of **BDP1** and **BisBDP1** is mainly located in the whole molecule in both the HOMO and LUMO, while the electron density of **BDP2** and **BisBDP2** is mainly located at the THQ units in the HOMO and the indacene plane in the LUMO, respectively. Notably, the electron density of **BisBDP1** and **BisBDP2** located at

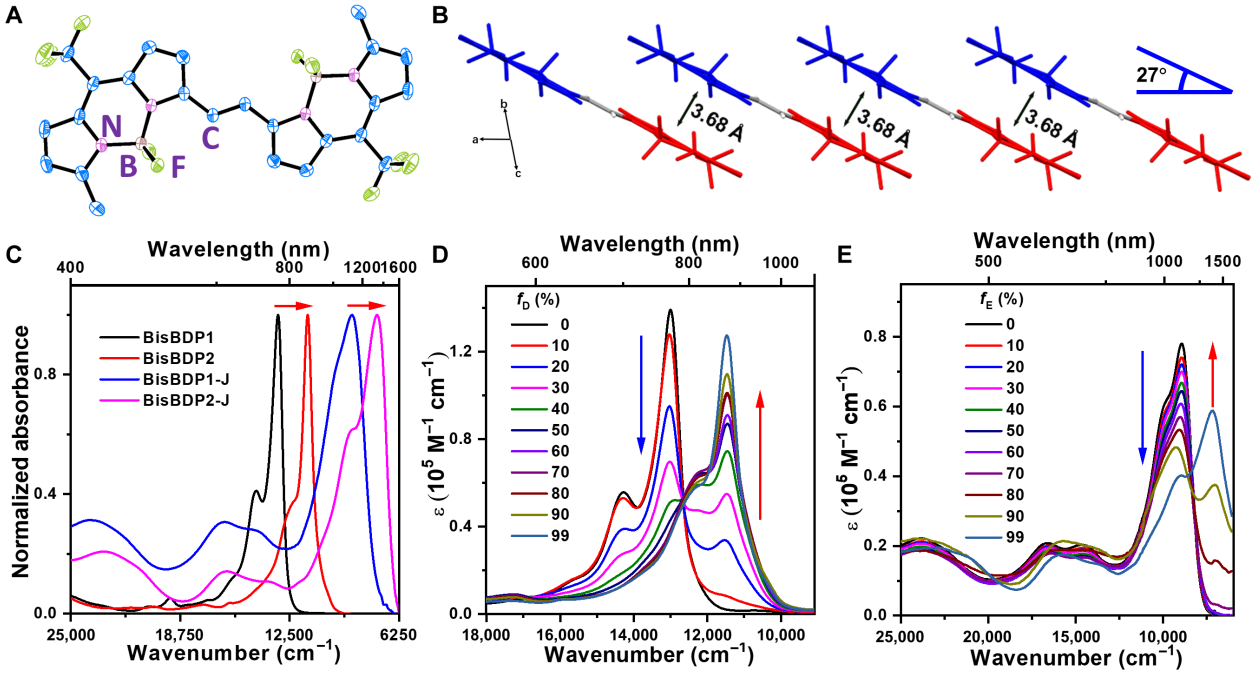

Fig. 2. Crystal structures and photophysical properties. (**A**) Crystal structures of **BisBDP1** (CCDC no. 2178500). H atoms are omitted for clarity. (**B**) J-type molecular packing diagrams of **BisBDP1** in the crystalline state. (**C**) Normalized absorption spectra of **BisBDP1**, **BisBDP2** in dichloromethane, and J-aggregates of **BisBDP1** and **BisBDP2** in DMF and ethanol. (**D** and **E**) J-aggregation behavior of **BisBDP1** [(D), 10 μM] in toluene–dimethyl formaldehyde (DMF) binary solvents with varied volumetric fractions of DMF (f_D) and **BisBDP2** [(E), 10 μM] in tetrahydrofuran-ethanol binary solvents with varied volumetric fractions of ethanol (f_E).

the ethenylene-bridge is around 6% in total in both HOMO and LUMO, which endows the delocalization of the electron density in the two indacene planes and narrows the bandgap. In addition, the decreased THQ unit and increased indacene plane contributions in LUMO expect the intramolecular CT character in **BDP2** and **BisBDP2**. Note that the electron density difference between the HOMO and LUMO of **BisBDP2** is less than that of **BDP2** (table S3), indicating the relatively weak CT character of **BisBDP2** than **BDP2**. This trend is consistent with the experiment results: The calculated transition dipole moment (μ_{eg}) value of **BisBDP2** is 7.9 D, which is smaller than those of **BDP2** (9.1 D). These results suggest that both the conjugation and push-pull effect dominated the large bathochromic shift of the λ_{abs}.

Photophysical properties of the J-aggregates

Before exploring the J-aggregation behavior, we first investigate their photophysical properties in organic solvents with different polarities (fig. S7). The absorption spectra of both **BDP1** and **BisBDP1** are stable in most organic solvents except for dimethyl formaldehyde (DMF) and dimethyl sulfide (DMSO), probably because of their relatively weak polar characteristic. In DMF and DMSO, **BDP1** is preferred to form H-aggregates with hypochromic-shifted λ_{abs} around 450 nm, which is consistent with the H-aggregation behavior of most BODIPY dyes (*31*, *32*). In contrast, **BisBDP1** tends to form aggregates in these two polar solvents, resulting in a sharp band centered at 873 nm with the full width at half maxima (FWHM) of 620 cm^{-1} and a shoulder band centered at 814 nm with FWHM 2000 cm^{-1}, respectively. The sharp absorption band should be attributed to J-aggregates with a highly ordered structure, while the broadband should be attributed to the monomeric absorption according to the following mechanism studies. Moreover, the notable narrowed and bathochromic-shifted J-band suggests the strong coupling between the monomers, resulting in extensive exciton states. The μ_{eg} increment from 7.1 of the monomer to 8.2 of the J-aggregates further confirms this speculation (table S2). Moreover, the coherence length N for the J-aggregates is estimated to be 10 according to the formula of $N = [(FW2/3)_M/(FW2/3)_J]^2$, whereas $(FW2/3)_M$ and $(FW2/3)_J$ are full width at two-thirds of the monomer and J-aggregates absorption bands (*48*, *49*). We also investigated the aggregation behavior of **BisBDP1** in toluene-DMF binary solvents, where toluene was used as a good solvent and DMF as a poor solvent (Fig. 2D). With the increment of the DMF fractions (f_D) in toluene, the monomeric absorption band centered at 769 nm decreased gradually, accompanied by increasing of the J-aggregate absorption bands. The absorption spectrum obtained with f_D = 99% is almost the same as that of obtained in DMF solution, which further confirmed the formation of J-aggregates.

Probably because of the good solubility in all organic solvents, **BDP2** retains the monomeric state, and its absorption band is slightly bathochromically shifted as organic solvent polarity increases (fig. S7B). In contrast, **BisBDP2** tends to J-aggregate in methanol and ethanol, and the λ_{abs} for the J-aggregates is around 1350 nm, respectively (fig. S7D). Compared with the monomer, J-aggregates formed in the ethanol showed the μ_{eg} increment from 6.8 to 8.0, and the narrowed FWHM from 1900 to 1410 cm^{-1}, which further indicates the formation of J-aggregates. The estimated coherence length (N) in methanol and ethanol is ≈4 and 2, respectively. The smaller N values than **BisBDP1** may be attributed to the increased molecular motion caused by the long alkyl chain and the increased molecular structure. Moreover, **BisBDP2** displayed expected J-aggregation

behavior in tetrahydrofuran (THF)–ethanol binary solvent, where THF was used as a good solvent and ethanol as a poor solvent. After adding ethanol to the THF solution of **BisBDP2**, the monomeric absorbance at 1125 nm (FWHM = 2600 cm^{-1}) decreased gradually with the ethanol volumetric factions (f_M) increased from 0 to 99%, accompanied by the appearance of a new J-band around 1375 nm with narrowed FWHM (1400 cm^{-1}). The absorption peak at 1125 nm still exists together with the band at 1365 nm, even with the f_M reaching 99%. This result is consistent with the monomeric absorption band observed in ethanol, implying that both the push-pull effect in the monomer and intermolecular J-coupling contributed to the absorption of **BisBDP2** J-aggregates (Fig. 2E).

Similar to the results obtained in the THF-ethanol binary solvent, the J-aggregation behavior of **BisBDP2** was also observed in the THF-water binary solvent. The addition of water into the THF solution of **BisBDP2** resulted in a new J-aggregation peak around 1276 nm, which is slightly hypochromic-shifted compared to that of in THF-ethanol binary solvent (fig. S8A). As water is more polar than ethanol, nonpolar long alkyl chains in **BisBDP2** are more likely to dissociate from water, which could result in a looser structure of **BisBDP2** J-aggregates in THF-water than in THF-ethanol. The less polar environment in which the J-aggregates form may suppress the CT effect and leads to hypsochromic-shifted absorption. In contrast to the excellent J-aggregation behavior in DMF, DMSO, and toluene-DMF binary solvents, **BisBDP1** tends to form H-aggregates in THF-water binary solvents with the water content reaching 99%. This result suggests that the J-aggregates of **BisBDP1** are difficult to stabilize in the THF-water binary system and that the **BisBDP1** molecule is more likely to produce kinetically controlled H-aggregates (fig. S9A). Next, we also investigated the salt effects on the J-aggregation of **BisBDP1** and **BisBDP2** in aqueous solutions. As shown in figs. S8 and S9, the absorption spectra of **BisBDP1** almost remain unchanged as the NaCl concentration is increased. While the absorption intensities of aggregates of **BisBDP2** decreased gradually because of the salting-out effect induced participation. Accordingly, NaCl has no promotion effect on the J-aggregation behavior of **BisBDP1** and **BisBDP2** probably due to their neutral chemical structures.

In the fluorescence spectra, the J-aggregates of **BisBDP1** and **BisBDP2** showed very weak fluorescence with λ_{em} around 982 and 1331 nm; however, the Φ_f of the J-aggregates are too low to be determined (fig. S10). The intramolecular CT effect and intermolecular π-π stacking may dominate the quenched fluorescence.

J-aggregation mechanistic studies

We carried out the temperature-dependent ultraviolet-visible (UV-vis)–NIR spectroscopic measurements and morphological studies to give insights into the mechanistic and structural details of the J-aggregates. With the temperature increasing from 283 to 343 K, both the J-bands of **BisBDP1** and **BisBDP2** in DMF and ethanol decrease gradually, accompanied by the increment of the monomeric absorption bands (Fig. 3, A and B). When the temperature reached 343 K, the J-bands disappeared, and only the absorption band of the monomer can be observed, which indicates the total dissociation of the J-aggregates to the monomers. Note that the absorbance of the shoulder band around 814 and 1125 nm for **BisBDP1** and **BisBDP2** did not decrease with increasing temperature. In contrast, these two shoulder bands gradually hypochromic-shifted and lastly converted to the monomeric absorption band. This result suggests that these two bands should be ascribed to the monomeric absorption rather than the aggregates without long-range order. We used the nucleation-elongation model to study the aggregation progress of **BisBDP1** and **BisBDP2** (*30*, *50*). After fitting the obtained UV-vis–NIR spectroscopic data of the fraction of aggregated molecules (α_{agg}) versus temperature (T; fig. S11), the molar enthalpy (ΔH_e) and elongation temperature (T_e) for the aggregation process were determined to be −23.4 KJ mol^{-1} and 340 *K* for **BisBDP1** and −50.0 KJ mol^{-1} and 343 K for **BisBDP2**, respectively. The lower ΔH_e of **BisBDP2** than that of **BisBDP1** suggests that **BisBDP2** is more preferred to aggregation than **BisBDP1**.

We further characterized the morphology of the J-aggregates by using atomic force microscopy. The drop-casting of the DMF solution of **BisBDP1** aggregates onto the surface of a silica wafer resulted in the deposition of rod-like aggregates (Fig. 3C) with a length of 880 ± 260 nm, a width of 240 ± 25 nm, and a height of 4.5 ± 0.3 nm, respectively. Under the same conditions, **BisBDP2** in ethanol solution self-assembled into round cake–like aggregates with a length of 600 ± 160 nm, a width of 350 ± 40 nm, and a height of 1.2 ± 0.1 nm, respectively (Fig. 3D). The larger conjugated structure of **BisBDP2** and the intramolecular motions and repulsion effect caused by the long alkyl chains may explain the difference in morphology between **BisBDP1** and **BisBDP2**. Moreover, these results further reveal that **BisBDP1** molecules are more likely to aggregate into a long-ranged molecule structure than **BisBDP2**, which is consistent with the estimated coherence length values obtained in the absorption spectra.

Photothermal and PA properties of the J-aggregates

In light of the above findings, J-aggregates of **BisBDP2** may prove useful as efficient NIR-II–absorbing PA imaging and photothermal agents because they exhibited strong absorption beyond 1200 nm and extremely low fluorescent quantum yield (*2*, *51*). Unfortunately, the poor fluorescence properties make **BisBDP2** J-aggregates unsuitable for fluorescence imaging. Next, we investigated the PA and photothermal properties of **BisBDP2** J-aggregates.

To achieve good stability and longtime blood circulation, we encapsulated **BisBDP2** J-aggregates into a Pluronic F-127 matrix to give water-soluble **BisBDP2** NPs (*5*, *34*). We found that a concentration range of 2 to 3 mg/ml was the best concentration for the preparation of the desired NPs (fig. S12). Transmission electron microscopy and dynamic light scattering analysis demonstrate that these NPs exist in a spherical morphology, and the diameter is around 100 nm (fig. S13). The small size endows the tumor accumulation potential of **BisBDP2** NPs through the enhanced permeability and retention effect (*52*). **BisBDP2** NPs showed λ_{abs} at 1273 nm (ε_{max} = 93000 M^{-1} cm^{-1}; Fig. 4A), which is consistent with that obtained in the THF-water binary solvents. This result suggests that **BisBDP2** J-aggregates are well stabilized in the Pluronic F-127 matrix. Notably, the high ε_{max} of **BisBDP2** NPs is comparable to the reported J-aggregates based on cyanine and squaraine (*7*, *26*, *28*), demonstrating the efficient photo absorption ability. **BisBDP2** NPs exhibited efficient photothermal conversion capability in phosphate-buffered saline (PBS) solution. After irradiation with 1208-nm (0.8 W cm^{-2}) laser light for 10 min, the temperature of the solution markedly increased from 28° to 62°C (ΔT = 34°C; Fig. 4, B and D). On the basis of the temperature change profiles, the photothermal conversion efficiency value was calculated to be 63%, which is comparable to that of reported NIR-II photothermal agents based on small organic molecules (*4*, *5*, *53*). Moreover, the temperature

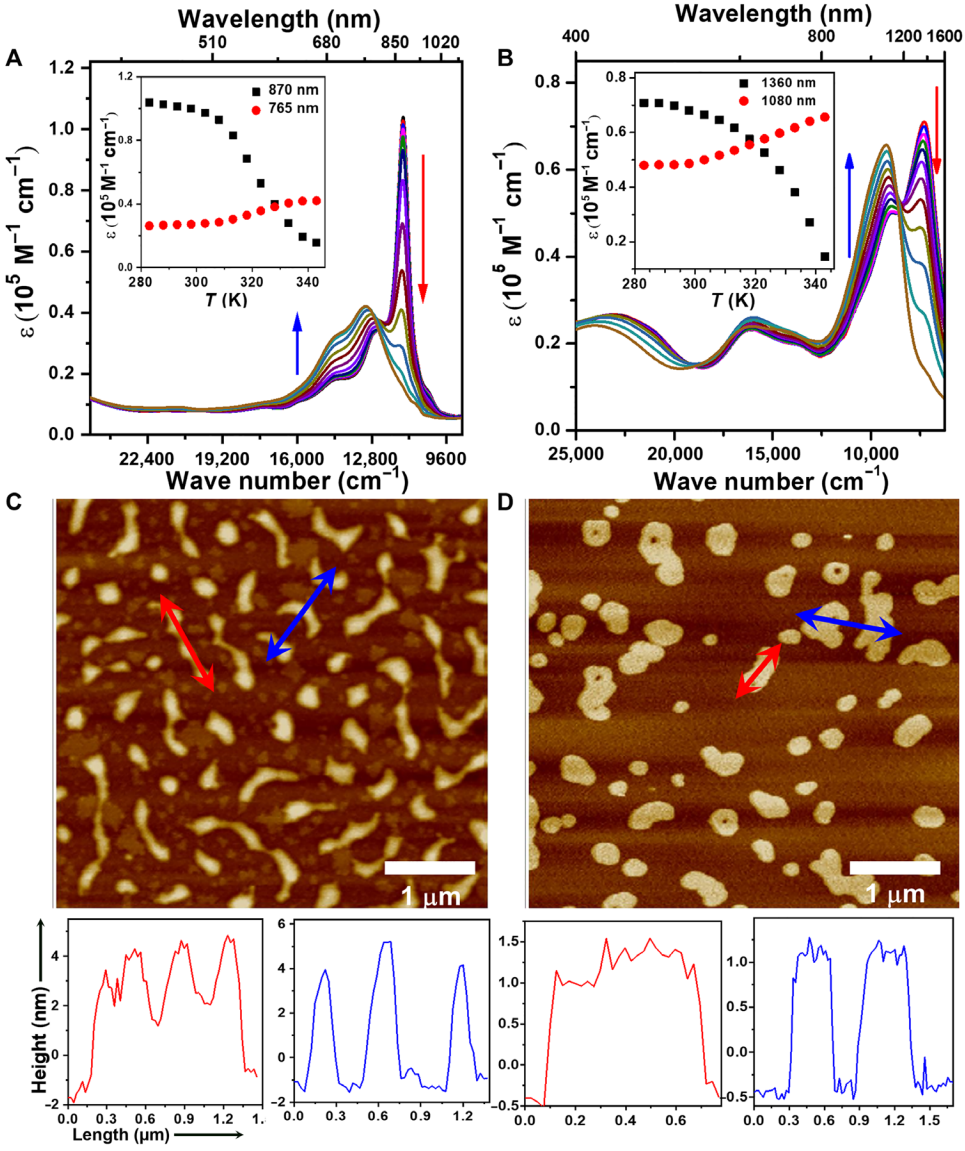

Fig. 3. Mechanism studies. Temperature-dependent absorption spectra of **BisBDP1** in DMF (**A**) **BisBDP2** in ethanol (**B**) from 283 to 343 K at a total concentration of 10 μM. Atomic force microscopy images of J-aggregates of **BisBDP1** (**C**) and **BisBDP2** (**D**) and cross-section analysis along the red and blue lines.

increment of **BisBDP2** NPs is positively related to the laser power density and the concentration of NPs (fig. S14), indicating the controllable photothermal conversion behavior. Furthermore, five heating and cooling cycles demonstrate the high thermal stability of **BisBDP2** NPs (Fig. 4C). As shown in figs. S15 and S16, the absorption spectra of **BisBDP2** in toluene and **BisBDP2** NPs in PBS remained almost unchanged under continuous laser irradiation for 1 hour, which demonstrates the good photostability of **BisBDP2** organic molecules and **BisBDP2** NPs. Besides, the UV-vis–NIR spectra of **BisBDP2** NPs remain almost unchanged over 8-hour storage in PBS buffer and fetal bovine serum, respectively, also proving their high stability.

As observed, **BisBDP2** NPs have superior photothermal conversion properties; thus, they should be applied to generate PA signals under laser irradiation. We therefore evaluated the in vitro PA imaging ability. Upon 1260-nm laser irradiation of an aqueous dispersion of **BisBDP2** NPs, actual acoustic waves from the NPs were detected (Fig. 4E). The resulting PA spectrum reveals the intense PA signals in the NIR-II window (fig. S17) and reflects the absorption spectrum very well. This result suggests that the intense NIR-II absorption of the J-aggregates governs the PA response. In addition, excellent correlation linearity is observed for the **BisBDP2** NP concentration versus PA intensity (fig. S18). Thus, the excellent PA response behavior makes sure that **BisBDP2** NPs could potentially be used for guiding the in vivo PTT.

In vitro photothermal properties

Because of the water absorption of NIR light and the thermal effect, 808- and 1064-nm lasers are currently commonly used for photoacoustic and photothermal experiments in the NIR-I and NIR-II

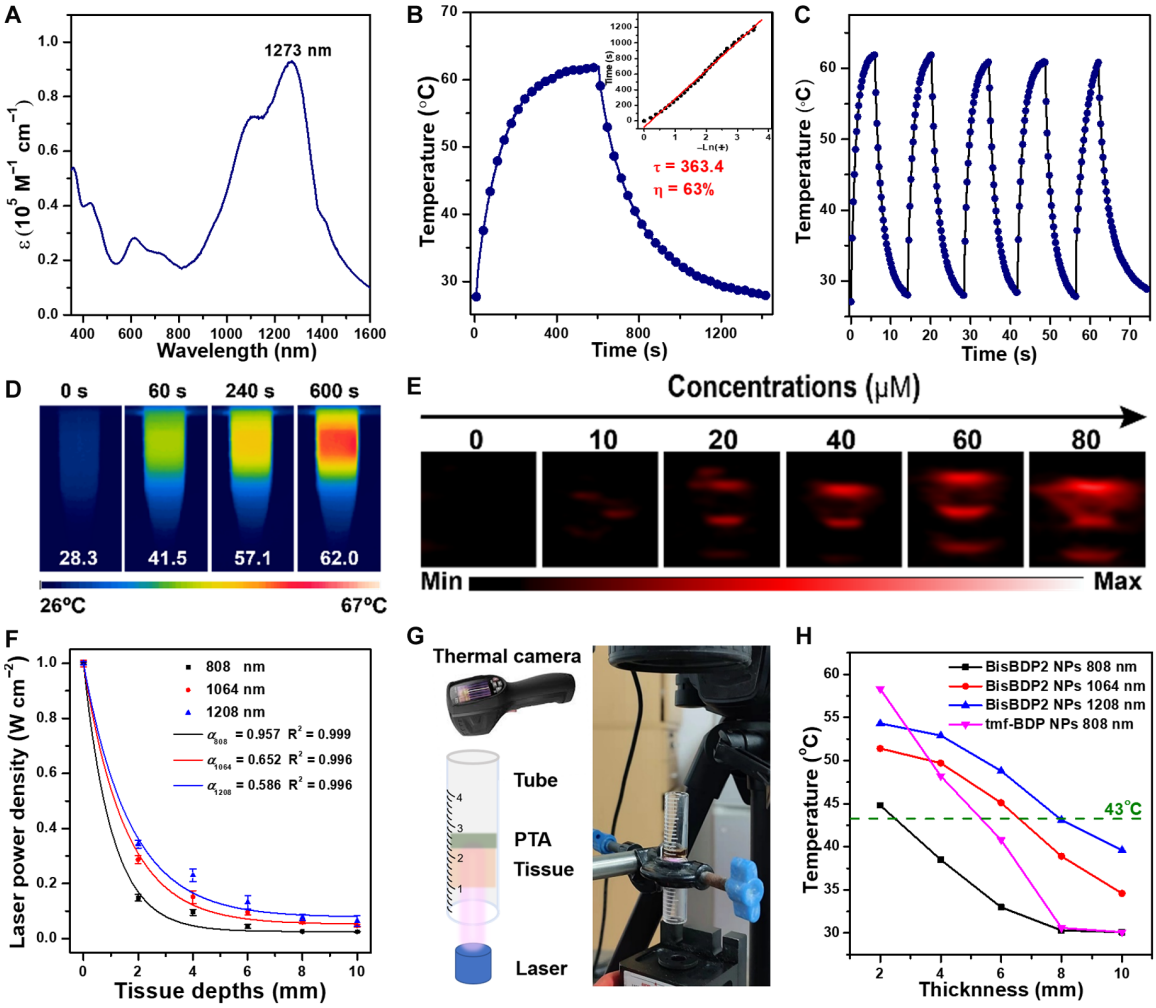

Fig. 4. In vitro PA and photothermal properties. (**A**) Absorbance spectrum of **BisBDP2** NPs in PBS solution. (**B**) Photothermic heating curves of **BisBDP2** NP dispersions under 1208-nm irradiation (0.8 W cm^{-2}) for 10 min followed by cooling to room temperature; Inset: Linear correlation of the cooling times versus negative natural logarithm of driving force temperatures. (**C**) Photothermic stability of **BisBDP2** NPs upon 1208-nm laser irradiation of 0.8 W cm^{-2} for five on/off cycles. (**D**) Infrared imaging of **BisBDP2** NP dispersions. (**E**) In vitro PA images of aqueous dispersions of **BisBDP2** NPs of different concentrations under 1260-nm irradiation. (**F**) Power density attenuation of the 808-, 1064-, and 1208-nm laser (1 W cm^{-2}) at different tissue depths. (**G**) Schematic diagram and equipment for the photothermal-conversion demonstration of different photothermal agents (PTAs; **BisBDP2** NPs and **tmf-BDP** NPs) by tissue-penetrated NIR laser (0.8 W cm^{-2}, 100 μM, and 200 μl). (**H**) Temperature changes of **BisBDP2** NPs and **tmf-BDP** NPs upon exposure to the tissue-penetrated laser via photothermal conversion.

windows, respectively. It is not known whether longer wavelength lasers can be used for in vivo experiments. In this study, we investigated the effects of different wavelengths of lasers on power density attenuation in different thicknesses of water and tissue (*54*) and revealed that the 1208-nm laser has the smallest power attenuation coefficient (α = 0.586) in tissue compared to 1064-nm (α = 0.652) and 808-nm (α = 0.957) lasers (Fig. 4F and fig. S19). We further evaluated the photothermal conversion ability of **BisBDP2** NPs in tissues of various thicknesses by irradiating **BisBDP2** NPs with different lasers (Fig. 4, G and H). At temperatures as high as 43°C, normal tissue is only mildly affected, and this temperature is capable of destroying tumors (*55*–*57*). Taking 43°C to be a reference temperature, **BisBDP2** NPs were irradiated with 808-, 1064-, and 1208-nm laser light through the tissue, and the thickness of the tissue was equal to 2, 6, and 8 mm, respectively. We also demonstrated that the NIR-I photothermal agent **tfm-BDP** (*58*), which has a high photothermal conversion efficiency of 88.3%, can reach a temperature of 43°C when the tissue penetrates 5 mm deep into the material. According to these results, it can be concluded that the 1208-nm laser has a better penetration depth in tissue compared to 1064- and 808-nm lasers. Therefore, we selected the 1208-nm laser as the light source for the follow-up in vivo and in vitro experiments.

Next, we investigated the PTT performance of **BisBDP2** NPs on living cells. **BisBDP2** NPs with various concentrations from 0 to 50 μM showed negligible toxicity to MCF-7, HeLa, and HepG2 cells, demonstrating good biosafety (fig. S20). After 1208-nm laser irradiation, about 90% of these cells can be efficiently killed through the photothermal effect. We also evaluated the photothermal effect of NPs on cell survival using a fluorescent imaging experiment (fig. S21). By costaining the calcein AM and propidium iodide dyes with the cancer cells, we found that the cells in the control group, the control + light group, and the NP group show green fluorescence,

indicating that these cells are in a normal live state. However, those cells incubated with NPs show red fluorescence after laser irradiating for 10 min, which suggests that the cells were efficiently killed by the thermal energy generated from the laser-activated NPs. All these cell results prove the good biocompatibility and efficient PTT performance of **BisBDP2** NPs.

We further investigated the pharmacokinetics of **BisBDP2** NPs in normal mice. As shown in fig. S22 and table S4, the blood NP concentration-time curves demonstrated that the concentration of **BisBDP2** NPs decayed rapidly at the initial stage, and the blood circulation half-time and clearance rate were calculated to be 7.4 hour and 8.0 liter hour^{-1}, respectively. These results indicate the excellent in vivo pharmacokinetic performance of **BisBDP2** NPs.

In vivo PA imaging

The above positive in vitro results prompted us to investigate the in vivo deep-tissue PTT performance of **BisBDP2** NPs. We established an orthotopic mouse model of hepatocellular carcinoma, which was confirmed by fluorescence imaging. Before the PTT investigation, we evaluated the in vivo PA imaging ability (Fig. 5A). Initially, the tumor-bearing liver site shows negligible PA signal at 1260 nm, which demonstrates the advantage of PA imaging beyond 1200 nm that can effectively avoid the PA signal interference generated by hemoglobin (*59*). After injecting the **BisBDP2** NPs (100 μM and 150 μl) to the mice through the tail vein, the PA signal intensity in the tumor site gradually increased to the maximum after 6-hour injection and then decreased gradually (Fig. 5B). Furthermore, we sacrificed the tumor-bearing mice and imaged the major organs via PA imaging to investigate the distribution of the **BisBDP2** NPs. The PA signals observed in the tumor are about 2.5, 2.1, 5.0, and 2.1 times higher than those in the heart, spleen, kidney, and liver (Fig. 5C and fig. S23), demonstrating the efficient tumor-specific accumulation of the NPs. For comparison, we also carried out the PA imaging experiment in normal mice (fig. S24). In the absence of **BisBDP2** NPs, normal mice also showed negligible PA signal in the liver site; however, the PA signal intensity distinctly increased to the maximum after 1-hour injection. This result indicates that the PA signals observed in the tumor-bearing group were located at the tumor site, which further verified the tumor-targeting and PA imaging capacities of **BisBDP2** NPs.

In vivo PTT

On the basis of the above PA imaging results, we performed the PTT experiments on the tumor-bearing mice. The mice were injected with the **BisBDP2** NPs in PBS solution at the tail vein and exposed to laser illumination at 1208 nm (0.8 W cm^{-2}). The liver site of the mice showed a gradual temperature increment from 30° to 49°C with the time increasing to 10 min. However, the mice in the control group only injected with PBS showed a slight temperature increment from 30°C to 36°C (Fig. 6, A and B). These results demonstrate the reliable in vivo photothermal conversion property of the NPs.

Next, we randomly divided these liver tumor–bearing mice into four groups (PBS, PBS + 1208-nm laser, **BisBDP2** NPs, **BisBDP2** NPs + 1208-nm laser) and monitored the tumor size through fluorescence imaging (Fig. 6C). During the 16-day treatment, the

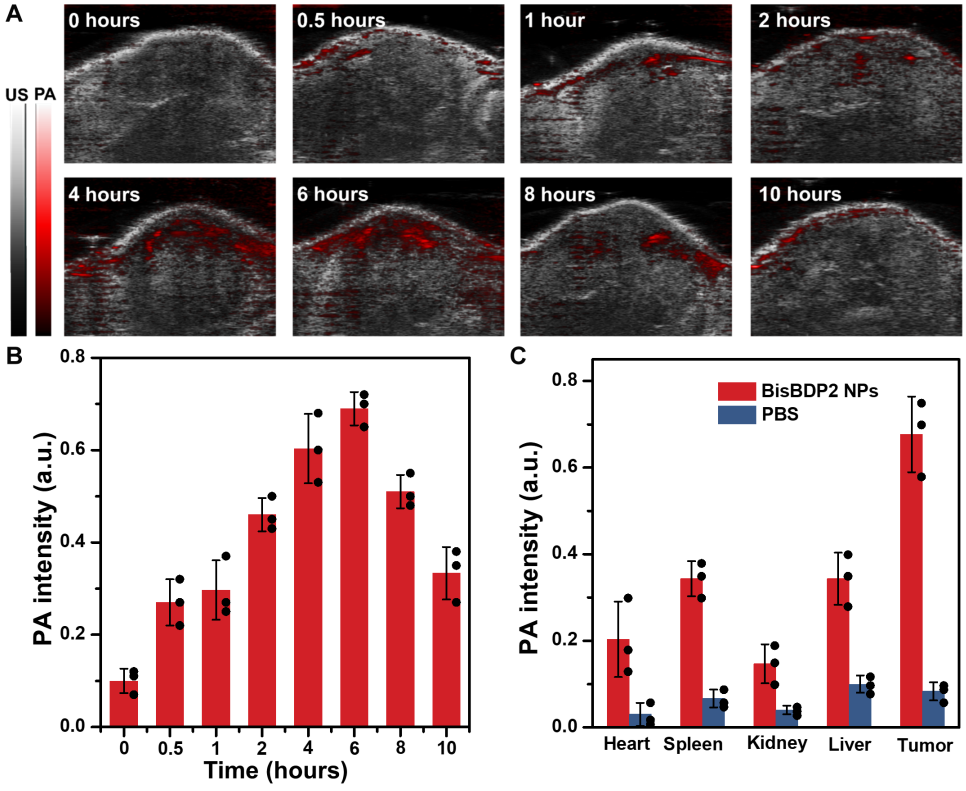

Fig. 5. PA imaging. (**A**) PA images of the orthotopic liver tumor at different times after injection of **BisBDP2** NPs at the tail vein. (**B**) PA intensity from (A) plotted as a function of time after injection. (**C**) The corresponding PA intensity from fig. S23.

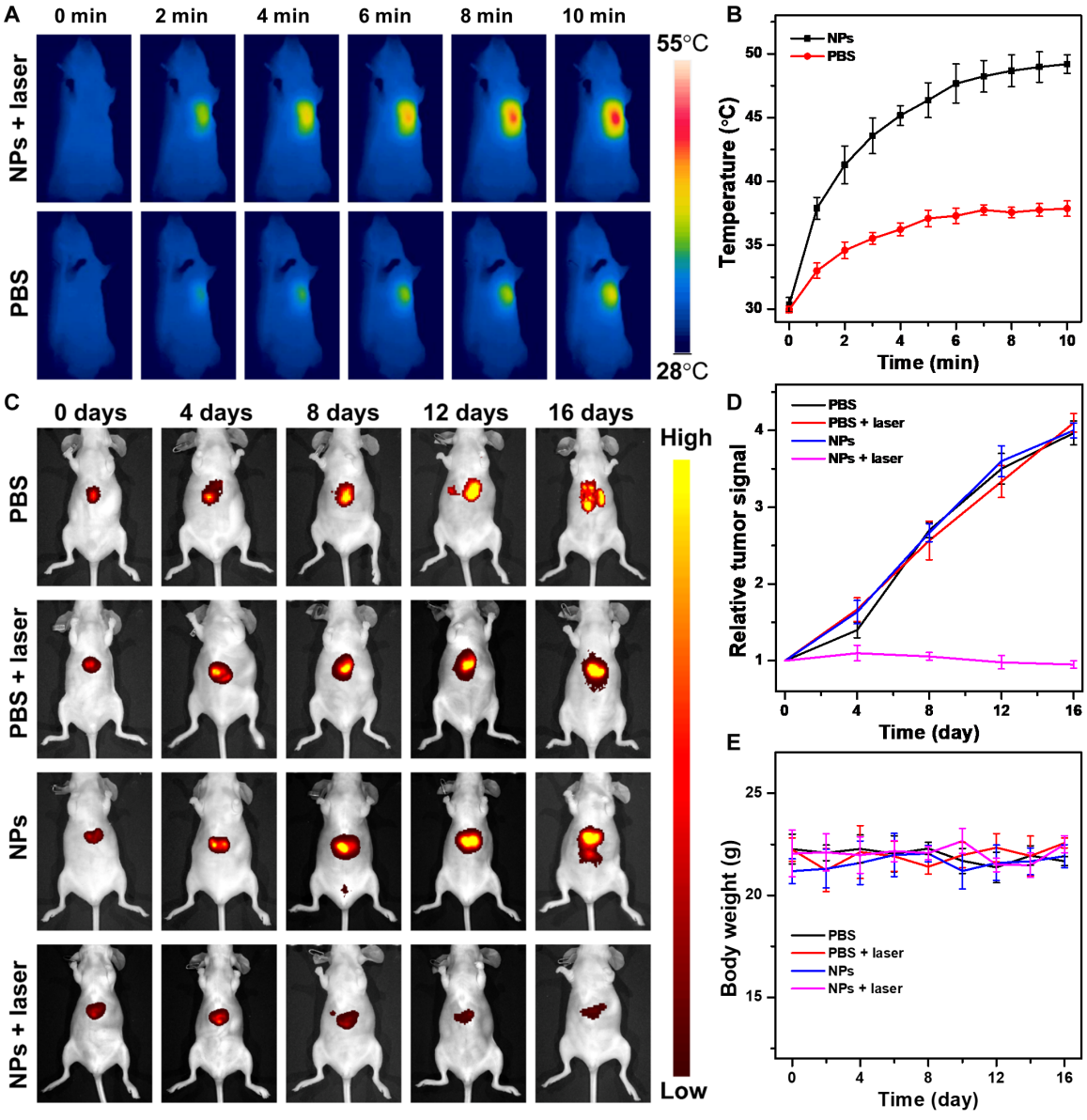

Fig. 6. In vivo PTT. (**A**) Infrared thermal imaging of orthotopic liver tumor mice treated with PBS and **BisBDP2** NPs exposed to 1208-nm laser (0.8 W cm^{-2}) recorded at different time intervals, respectively. (**B**) Temperature profiles of tumor site as a function of irradiation time. (**C**) Fluorescence images of the mice treated with PBS, NPs, PBS + 1208-nm laser, and NPs + 1208-nm laser on days 0, 4, 8, 12, and 16, respectively (data are means ± SEM, $n = 3$). (**D**) Relative orthotopic liver tumor fluorescence intensity of the mice and (**E**) body weight changes of mice during different treatments.

relative tumor signals shown in the PBS, PBS + 1208-nm laser, and **BisBDP2** NP groups were linearly increased, and the final volume is about fourfold than the initial one, indicating the fast proliferation of the tumor. In contrast, the relative tumor signals in the **BisBDP2** NPs + 1208-nm laser group gradually decreased from 1.0 to 0.95, demonstrating an efficient suppressive effect on tumor proliferation (Fig. 6D). In addition, the results of tissue anatomy show that the volume of the tumors is the smallest among all the four groups, which are consistent with those observed in the bioimaging experiments (fig. S25). During the treatment, the mice body weight in the four groups is stable, which further indicates the high biocompatibility of the **BisBDP2** NPs (Fig. 6E). Furthermore, we evaluated the tumor apoptosis through hematoxylin and eosin (H&E; fig. S26) and terminal deoxynucleotidyl transferase–mediated deoxyuridine triphosphate nick end labeling (TUNEL; fig. S27) staining. The cells in the heart, kidney, and lung showed negligible change in the four groups, demonstrating the minimal toxicity of the NPs. Notably, the necrotic regions in the tumor cells are visible in the **BisBDP2** NPs + 1208-nm laser group but not in other groups. These results revealed the favorable biological safety and excellent in vivo PTT efficacy of **BisBDP2** NPs in the NIR-II window.

DISCUSSION

We have designed and synthesized donor-acceptor–structured ethenylene-bridged BODIPY dye for the generation of J-aggregates

with λ_{abs} beyond 1200 nm. The ethenylene-bridged BODIPY dye showed the λ_{abs} at 1100 nm in dichloromethane solution, which suggests that the combination of push-pull and conjugation effect to the BODIPY-dimer could be an efficient way to design NIR-II–absorbing BODIPY dyes. Moreover, the zig-zag structure of the BODIPY dimer endows the efficient J-aggregation behavior in organic binary solvents, resulting in further bathochromic-shifted λ_{abs} approximately at 1300 nm. Notably, the J-aggregates can be generated in water solution and stabilized in the Pluronic F-127 polymer matrix. The J-aggregates showed very weak fluorescence, facilitating the high PCE value of 63% under 1208-nm laser irradiation (0.8 W cm^{-2}). In vitro and in vivo studies revealed excellent biocompatibility, NIR-II PA imaging ability for tumor diagnosis, and high PTT performance for orthotopic hepatocellular carcinoma. Consequently, our findings demonstrate that J-aggregates of ethenylene-bridged BODIPY dye have great promise as a scaffold for developing NIR-II–absorbing photothermal agents, and the present study offers an alternative strategy to explore organic NIR-II–absorbing agents for biophotonics applications.

MATERIALS AND METHODS

NP preparation

BisBDP2 (2 mg) was dissolved in THF (1 ml) by bath sonication. Fifteen milligrams of Pluronic F-127 was dissolved in 1 ml of **BisBDP2** stock solution and then the solutions were quickly added to 5 ml of PBS buffer containing 20% ethanol and dispersed by vibration for 30 min under ultrasound. After dispersion, THF and ethanol were removed under reduced pressure. Then, the solutions were filtered through a 0.2-μm syringe filter; the NP suspension was obtained and stored at 4°C for further use.

Photophysical properties

UV-vis and UV-vis–NIR absorption spectra were respectively measured at room temperature on a Shimadzu UV-1750 spectrometer and a Shimadzu UV-3600 spectrophotometer with a resolution of 1.0 nm, using quartz cuvettes of 1.0-cm path length. The full absorbance spectrum of **BisBDP2** NPs in PBS (300 to 1600 nm) was obtained by using quartz cuvettes of 0.5-cm path length. Fluorescence spectra of **BDP1** were measured on a FLUOROMAX-4 spectrometer under an air atmosphere at room temperature; Fluorescent spectra of **BDP2** and **BisBDP1** were recorded using an Edinburgh FLSP920 fluorescence spectrophotometer equipped with a microsecond flash-lamp (UF900). NIR-II fluorescence spectra of **BisBDP2** were recorded on a three-dimensional fluorescence spectrometer at room temperature.

Animals and tumor-bearing mouse model

All animal studies were conducted by the guidelines set by the Jiangsu Committee of Use and Care of Laboratory Animals and under protocols approved by the Animal Ethics Committee in Nanjing University [SCXK(Su)-2020-0009] and the National Institutes of Health Clinical Center Animal Care and Use Committee. Five-week-old female orthotopic liver tumor with red fluorescent protein (RFP; Ex, 560 nm; Em, 620 nm) mice were purchased from the Nanjing Junke Biotechnology Co. Ltd., China. Relative tumor volume was examined using fluorescence imaging in vivo. Methods for establishing an orthotopic tumor-bearing mouse model: Human hepatocellular carcinoma cells labeled with an RFP (Hep G2-RFP) were inoculated into the right subcutis of BALB/C female nude mice. When the volume of Hep G2-RFP subcutaneous tumor grew to about 500 mm^3, the subcutaneous tumor was peeled off and then divided into 1 mm by 1 mm by 1 mm tumor tissue blocks in the culture medium, and the tumor tissue blocks were transplanted into the liver of nude mice using surgical procedures.

PA imaging

To evaluate the PA imaging performance, a PA computed tomography was performed on a Vevo LAZR-X system (FUJIFILM VisualSonics, America). First, the NPs at various concentration were used to examine PA signals and their linear relation. For in vivo PA imaging, the orthotopic liver tumor–bearing mice and normal mice were intravenously injected with 150 μl of **BisBDP2** NP solution (100 μM) and then the PA signal of the tumor and liver site was observed under a multispectral PA tomography instrument as a function of past injection times (0, 0.5, 1, 2, 4, 6, 8, and 10 hours) with an excitation wavelength of 1260 nm. Last, we investigated the biodistribution of **BisBDP2** NPs. After the injection for 6 hours, the orthotopic liver tumor–bearing mice were euthanized and their major organs containing the heart, spleen, kidney liver, and tumor were isolated and imaged (n = 3 per group).

In vivo PTT

An orthotopic liver tumor with an RFP model was established to confirm the in vivo deep-tissue therapeutic efficacy of **BisBDP2** NPs after 1208-nm laser exposure. The liver tumor–bearing mice with fluorescence signals were randomly divided into four groups (n = 3 per group), named "PBS," "NPs," "PBS + 1208-nm laser," and "NPs + 1208-nm laser," respectively. Solution (150 μl) was injected into the tumor-bearing mice through a tail vein using a microsyringe. For PBS + 1208-nm laser and NPs + 1208-nm laser groups, after intravenous injection of saline and **BisBDP2** NPs (100 μM and 150 μl) for 4 hours, respectively, the tumors of mice in each group were continuously irradiated with a 1208-nm laser (0.8 W cm^{-2}) for 10 min. In the meantime, the temperature changes of the tumors were recorded every 10 s via an IR thermal camera. After a variety of treatments, the tumor volumes were measured every 4 days by fluorescence signal, and mouse body weights were measured every other day during the 16-day study duration.

Histomorphology analysis

After 16 days of various treatments, the abovementioned four groups of mice were sacrificed. The lung, kidney, heart, and tumor were excised, fixed in 4% formalin solution, and sectioned at 5-μm thickness. After conventional H&E staining, the slices were examined with a digital microscope (Leica QWin). The fluorescent TUNEL staining was conducted following the manual instruction of the DeadEnd fluorometric TUNEL system Kit (Promega, USA). The nuclei were counterstained with 4′,6-diamidino-2-phenylindole.

SUPPLEMENTARY MATERIALS

Supplementary material for this article is available at https://science.org/doi/10.1126/sciadv.add5660

REFERENCES AND NOTES

1. C. Kim, C. Favazza, L. V. Wang, In vivo photoacoustic tomography of chemicals: High-resolution functional and molecular optical imaging at new depths. *Chem. Rev.* **110**, 2756–2782 (2010).

2. H. S. Jung, P. Verwilst, A. Sharma, J. Shin, J. L. Sessler, J. S. Kim, Organic molecule-based photothermal agents: An expanding photothermal therapy universe. *Chem. Soc. Rev.* **47**, 2280–2297 (2018).
3. J. Chen, A. C. Sedgwick, S. Sen, Y. Ren, Q. Sun, C. Chau, J. F. Arambula, T. Sarma, L. Song, J. L. Sessler, C. Liu, Expanded porphyrins: Functional photoacoustic imaging agents that operate in the NIR-II region. *Chem. Sci.* **12**, 9916–9921 (2021).
4. S. Li, Q. Deng, Y. Zhang, X. Li, G. Wen, X. Cui, Y. Wan, Y. Huang, J. Chen, Z. Liu, L. Wang, C.-S. Lee, Rational design of conjugated small molecules for superior photothermal theranostics in the NIR-II biowindow. *Adv. Mater.* **32**, 2001146 (2020).
5. Z. Jiang, C. Zhang, X. Wang, M. Yan, Z. Ling, Y. Chen, Z. Liu, A borondifluoride-complex-based photothermal agent with an 80% photothermal conversion efficiency for photothermal therapy in the NIR-II window. *Angew. Chem. Int. Ed.* **60**, 22376–22384 (2021).
6. E. D. Cosco, A. L. Spearman, S. Ramakrishnan, J. G. P. Lingg, M. Saccomano, M. Pengshung, B. A. Arus, K. C. Y. Wong, S. Glasl, V. Ntziachristos, M. Warmer, R. R. McLaughlin, O. T. Bruns, E. M. Sletten, Shortwave infrared polymethine fluorophores matched to excitation lasers enable non-invasive, multicolour in vivo imaging in real time. *Nat. Chem.* **12**, 1123–1130 (2020).
7. C. Sun, B. Li, M. Zhao, S. Wang, Z. Lei, L. Lu, H. Zhang, L. Feng, C. Dou, D. Yin, H. Xu, Y. Cheng, F. Zhang, *J*-aggregates of cyanine dye for NIR-II in vivo dynamic vascular imaging beyond 1500 nm. *J. Am. Chem. Soc.* **141**, 19221–19225 (2019).
8. Z. Lei, C. Sun, P. Pei, S. Wang, D. Li, X. Zhang, F. Zhang, Stable, wavelength-tunable fluorescent dyes in the NIR-II region for in vivo high-contrast bioimaging and multiplexed biosensing. *Angew. Chem. Int. Ed.* **58**, 8166–8171 (2019).
9. R. Tian, Q. Zeng, S. Zhu, J. Lau, S. Chandra, R. Ertsey, K. S. Hettie, T. Teraphongphom, Z. Hu, G. Niu, D. O. Kiesewetter, H. Sun, X. Zhang, A. L. Antaris, B. R. Brooks, X. Chen, Albumin-chaperoned cyanine dye yields superbright NIR-II fluorophore with enhanced pharmacokinetics. *Sci. Adv.* **5**, eaaw0672 (2019).
10. M. M. M. Swamy, Y. Murai, K. Monde, S. Tsuboi, T. Jin, Shortwave-infrared fluorescent molecular imaging probes based on π-conjugation extended indocyanine green. *Bioconjug. Chem.* **32**, 1541–1547 (2021).
11. W. Xu, E. Leary, S. Sangtarash, M. Jirasek, M. T. Gonzalez, K. E. Christensen, L. A. Vicente, N. Agrait, S. J. Higgins, R. J. Nichols, C. J. Lambert, H. L. Anderson, A peierls transition in long polymethine molecular wires: Evolution of molecular geometry and single-molecule conductance. *J. Am. Chem. Soc.* **143**, 20472–20481 (2021).
12. B. Li, L. Lu, M. Zhao, Z. Lei, F. Zhang, An efficient 1064 nm NIR-II excitation fluorescent molecular dye for deep-tissue high-resolution dynamic bioimaging. *Angew. Chem. Int. Ed.* **57**, 7483–7487 (2018).
13. D. Ndaleh, C. Smith, M. Loku Yaddehige, A. K. Shaik, D. L. Watkins, N. I. Hammer, J. H. Delcamp, Shortwave infrared absorptive and emissive pentamethine-bridged indolizine cyanine dyes. *J. Org. Chem.* **86**, 15376–15386 (2021).
14. H. Zhou, X. Zeng, A. Li, W. Zhou, L. Tang, W. Hu, Q. Fan, X. Meng, H. Deng, L. Duan, Y. Li, Z. Deng, X. Hong, Y. Xiao, Upconversion NIR-II fluorophores for mitochondria-targeted cancer imaging and photothermal therapy. *Nat. Commun.* **11**, 6183 (2020).
15. R. S. Rao, Suman, S. P. Singh, Near-infrared (>1000 nm) light-harvesters: Design, synthesis and applications. *Chem. Eur. J.* **26**, 16582–16593 (2020).
16. V. V. Diev, K. Hanson, J. D. Zimmerman, S. R. Forrest, M. E. Thompson, Fused pyrene-diporphyrins: Shifting near-infrared absorption to 1.5 microm and beyond. *Angew. Chem. Int. Ed.* **49**, 5523–5526 (2010).
17. M. Tian, S. Tatsuura, M. Furuki, Y. Sato, I. Iwasa, L. S. Pu, Discovery of novel dyes with absorption maxima at 1.1 μm. *J. Am. Chem. Soc.* **125**, 348–349 (2003).
18. B. Ding, Y. Xiao, H. Zhou, X. Zhang, C. Qu, F. Xu, Z. Deng, Z. Cheng, X. Hong, Polymethine thiopyrylium fluorophores with absorption beyond 1000 nm for biological imaging in the second near-infrared subwindow. *J. Med. Chem.* **62**, 2049–2059 (2019).
19. Q. Wu, Z. Kang, Q. Gong, X. Guo, H. Wang, D. Wang, L. Jiao, E. Hao, Strategic construction of ethene-bridged BODIPY arrays with absorption bands reaching the near-infrared II region. *Org. Lett.* **22**, 7513–7517 (2020).
20. T. B. Ren, Z. Y. Wang, Z. Xiang, P. Lu, H. H. Lai, L. Yuan, X. B. Zhang, W. Tan, A general strategy for development of activatable NIR-II fluorescent probes for in vivo high-contrast bioimaging. *Angew. Chem. Int. Ed.* **60**, 800–805 (2021).
21. D. Liu, Z. He, Y. Zhao, Y. Yang, W. Shi, X. Li, H. Ma, Xanthene-based NIR-II dyes for in vivo dynamic imaging of blood circulation. *J. Am. Chem. Soc.* **143**, 17136–17143 (2021).
22. H. C. Daly, S. S. Matikonda, H. C. Steffens, B. Ruehle, U. Resch-Genger, J. Ivanic, M. J. Schnermann, Ketone incorporation extends the emission properties of the xanthene scaffold beyond 1000 nm. *Photochem. Photobiol.* **98**, 325–333 (2022).
23. J. Gayton, S. A. Autry, W. Meador, S. R. Parkin, G. A. Hill Jr., N. I. Hammer, J. H. Delcamp, Indolizine-cyanine dyes: Near infrared emissive cyanine dyes with increased stokes shifts. *J. Org. Chem.* **84**, 687–697 (2019).
24. F. Würthner, T. E. Kaiser, C. R. Saha-Moller, J-aggregates: From serendipitous discovery to supramolecular engineering of functional dye materials. *Angew. Chem. Int. Ed.* **50**, 3376–3410 (2011).
25. D. Miranda, H. Huang, H. Kang, Y. Zhan, D. Wang, Y. Zhou, J. Geng, H. I. Kilian, W. Stiles, A. Razi, J. Ortega, J. Xia, H. S. Choi, J. F. Lovell, Highly-soluble cyanine J-aggregates entrapped by liposomes for in vivo optical imaging around 930 nm. *Theranostics* **9**, 381–390 (2019).
26. W. Chen, C. A. Cheng, E. D. Cosco, S. Ramakrishnan, J. G. P. Lingg, O. T. Bruns, J. I. Zink, E. M. Sletten, Shortwave infrared imaging with J-aggregates stabilized in hollow mesoporous silica nanoparticles. *J. Am. Chem. Soc.* **141**, 12475–12480 (2019).
27. C. Sun, M. Zhao, X. Zhu, P. Pei, F. Zhang, One-pot preparation of highly dispersed second near-infrared J-aggregate nanoparticles based on FD-1080 cyanine dye for bioimaging and biosensing. *Chin. Chem. Soc. Publ.* **3**, 3060–3070 (2021).
28. C. A. Shen, M. Stolte, J. H. Kim, A. Rausch, F. Würthner, Double J-coupling strategy for near infrared emitters. *J. Am. Chem. Soc.* **143**, 11946–11950 (2021).
29. H. Lu, J. Mack, Y. Yang, Z. Shen, Structural modification strategies for the rational design of red/NIR region BODIPYs. *Chem. Soc. Rev.* **43**, 4778–4823 (2014).
30. Z. Chen, Y. Liu, W. Wagner, V. Stepanenko, X. Ren, S. Ogi, F. Würthner, Near-IR absorbing J-aggregate of an amphiphilic BF_2-azadipyrromethene dye by kinetic cooperative self-assembly. *Angew. Chem. Int. Ed.* **56**, 5729–5733 (2017).
31. S. Choi, J. Bouffard, Y. Kim, Aggregation-induced emission enhancement of a *meso*-trifluoromethyl BODIPY via J-aggregation. *Chem. Sci.* **5**, 751–755 (2014).
32. S. Kim, J. Bouffard, Y. Kim, Tailoring the solid-state fluorescence emission of BODIPY dyes by *meso* substitution. *Chem. A Eur. J.* **21**, 17459–17465 (2015).
33. L. J. Patalag, L. P. Ho, P. G. Jones, D. B. Werz, Ethylene-bridged oligo-BODIPYs: Access to intramolecular J-aggregates and superfluorophores. *J. Am. Chem. Soc.* **139**, 15104–15113 (2017).
34. K. Li, X. Duan, Z. Jiang, D. Ding, Y. Chen, G. Q. Zhang, Z. Liu, J-aggregates of *meso*-[2.2] paracyclophanyl-BODIPY dye for NIR-II imaging. *Nat. Commun.* **12**, 2376 (2021).
35. Y. Chen, X. H. Zhang, D. B. Cheng, Y. Zhang, Y. Liu, L. Ji, R. Guo, H. Chen, X. K. Ren, Z. Chen, Z. Y. Qiao, H. Wang, Near-infrared laser-triggered in situ dimorphic transformation of BF_2-azadipyrromethene nanoaggregates for enhanced solid tumor penetration. *ACS Nano* **14**, 3640–3650 (2020).
36. H. He, S. Ji, Y. He, A. Zhu, Y. Zou, Y. Deng, H. Ke, H. Yang, Y. Zhao, Z. Guo, H. Chen, Photoconversion-tunable fluorophore vesicles for wavelength-dependent photoinduced cancer therapy. *Adv. Mater.* **29**, (2017).
37. M. H. Y. Cheng, K. M. Harmatys, D. M. Charron, J. Chen, G. Zheng, Stable J-aggregation of an aza-BODIPY-lipid in a liposome for optical cancer imaging. *Angew. Chem. Int. Ed.* **58**, 13394–13399 (2019).
38. Q. Zhang, P. Yu, Y. Fan, C. Sun, H. He, X. Liu, L. Lu, M. Zhao, H. Zhang, F. Zhang, Bright and stable NIR-II J-aggregated AIE diBODIPY-based fluorescent probe for dynamic in vivo bioimaging. *Angew. Chem. Int. Ed.* **60**, 3967–3973 (2021).
39. X. Guo, M. Li, H. Wu, W. Sheng, Y. Feng, C. Yu, L. Jiao, E. Hao, Near-ir absorbing J-aggregates of a phenanthrene-fused BODIPY as a highly efficient photothermal nanoagent. *Chem. Commun.* **56**, 14709–14712 (2020).
40. M. Su, S. Li, H. Zhang, J. Zhang, H. Chen, C. Li, Nano-assemblies from J-aggregated dyes: A stimuli-responsive tool applicable to living systems. *J. Am. Chem. Soc.* **141**, 402–413 (2019).
41. J. Xia, Z. Li, Z. Xie, M. Zheng, Near-infrared absorbing J-aggregates of boron dipyrromethene for high efficient photothermal therapy. *J. Colloid Interface Sci.* **599**, 476–483 (2021).
42. M. Su, Q. Han, X. Yan, Y. Liu, P. Luo, W. Zhai, Q. Zhang, L. Li, C. Li, A supramolecular strategy to engineering a non-photobleaching and near-infrared absorbing nano-J-aggregate for efficient photothermal therapy. *ACS Nano* **15**, 5032–5042 (2021).
43. M. L. Picchio, J. Bergueiro, S. Wedepohl, R. J. Minari, C. I. A. Igarzabal, L. M. Gugliotta, J. C. Cuggino, M. Calderon, Exploiting cyanine dye J-aggregates/monomer equilibrium in hydrophobic protein pockets for efficient multi-step phototherapy: An innovative concept for smart nanotheranostics. *Nanoscale* **13**, 8909–8921 (2021).
44. C. C. L. Cheung, G. Ma, K. Karatasos, J. Seitsonen, J. Ruokolainen, C. R. Koffi, H. Hassan, W. T. Al-Jamal, Liposome-templated indocyanine green J- aggregates for in vivo near infrared imaging and stable photothermal heating. *Nanotheranostics* **4**, 91–106 (2020).
45. S. Ye, J. Rao, S. Qiu, J. Zhao, H. He, Z. Yan, T. Yang, Y. Deng, H. Ke, H. Yang, Y. Zhao, Z. Guo, H. Chen, Rational design of conjugated photosensitizers with controllable photoconversion for dually cooperative phototherapy. *Adv. Mater.* **30**, e1801216 (2018).
46. J. Ahrens, B. Haberlag, A. Scheja, M. Tamm, M. Broring, Conjugated BODIPY dyemers by metathesis reactions. *Chem. A Eur. J.* **20**, 2901–2912 (2014).
47. R. Misra, S. P. Bhattacharyya, *Intramolecular Charge Transfer: Theory and Applications* (Wiley-VCH, ed. 1, 2018).
48. E. W. Knapp, Lineshapes of molecular aggregates, exchange narrowing and intersite correlation. *Chem. Phys.* **85**, 73–82 (1984).
49. N. Vranken, M. Van der Auweraer, F. C. De Schryver, H. Lavoie, P. Bélanger, C. Salesse, Influence of molecular structure on the aggregating properties of thiacarbocyanine dyes adsorbed to langmuir films at the air–water interface. *Langmuir* **16**, 9518–9526 (2000).
50. P. Jonkheijm, P. van der Schoot, A. P. Schenning, E. W. Meijer, Probing the solvent-assisted nucleation pathway in chemical self-assembly. *Science* **313**, 80–83 (2006).

51. H. Ding, Q. Shen, J. Shao, W. Wang, F. Gao, X. Dong, Small molecular NIR-II fluorophores for cancer phototheranostics. *Innovation* **2**, 100082 (2021).
52. K. Greish, Enhanced permeability and retention (epr) effect for anticancer nanomedicine drug targeting. *Methods Mol. Biol.* **624**, 25–37 (2010).
53. H. Xiang, L. Zhao, L. Yu, H. Chen, C. Wei, Y. Chen, Y. Zhao, Self-assembled organic nanomedicine enables ultrastable photo-to-heat converting theranostics in the second near-infrared biowindow. *Nat. Commun.* **12**, 218 (2021).
54. H. Lin, S. Gao, C. Dai, Y. Chen, J. Shi, A two-dimensional biodegradable niobium carbide (Mxene) for photothermal tumor eradication in NIR-I and NIR-II biowindows. *J. Am. Chem. Soc.* **139**, 16235–16247 (2017).
55. M. Hiraoka, S. Jo, K. Akuta, Y. Nishimura, M. Takahashi, M. Abe, Radiofrequency capacitive hyperthermia for deep-seated tumors. I. Studies on thermometry. *Cancer* **60**, 121–127 (1987).
56. W. C. Dewey, Arrhenius relationships from the molecule and cell to the clinic. *Int. J. Hyperthermia* **25**, 3–20 (2009).
57. M. W. Dewhirst, B. L. Viglianti, M. Lora-Michiels, M. Hanson, P. J. Hoopes, Basic principles of thermal dosimetry and thermal thresholds for tissue damage from hyperthermia. *Int. J. Hyperthermia* **19**, 267–294 (2003).
58. D. Xi, M. Xiao, J. Cao, L. Zhao, N. Xu, S. Long, J. Fan, K. Shao, W. Sun, X. Yan, X. Peng, NIR light-driving barrier-free group rotation in nanoparticles with an 88.3% photothermal conversion efficiency for photothermal therapy. *Adv. Mater.* **32**, e1907855 (2020).
59. K. Haedicke, L. Agemy, M. Omar, A. Berezhnoi, S. Roberts, C. Longo-Machado, M. Skubal, K. Nagar, H. T. Hsu, K. Kim, T. Reiner, J. Coleman, V. Ntziachristos, A. Scherz, J. Grimm, High-resolution optoacoustic imaging of tissue responses to vascular-targeted therapies. *Nat. Biomed. Eng.* **4**, 286–297 (2020).
60. V. Leen, T. Leemans, N. Boens, W. Dehaen, 2- and 3-monohalogenated BODIPY dyes and their functionalized analogues: Synthesis and spectroscopy. *European J. Org. Chem.* **2011**, **2011**, 4386–4396

Acknowledgments

Funding: This work was supported by National Natural Science Foundation of China grant 21971115 and Natural Science Foundation of Jiangsu Province (BK20221333). **Author contributions:** Conceptualization: X.W., Z.J., and Z. Liu. Methodology: X.W., Z.J., Z. Lia., and T.W. Investigation: X.W., Z.J., Z. Lia., and T.W. Supervision: Z. Liu Writing (original draft): X.W., Z.J., and Z. Liu Writing (review and editing): X.W., Z.J., Y.C., and Z. Liu **Competing interests:** The authors declare that they have no competing interests. **Data and materials availability:** All data needed to evaluate the conclusions in the paper are present in the paper and/or the Supplementary Materials. The x-ray crystallographic coordinates for the structures reported in this article have been deposited at the Cambridge Crystallographic Data Centre (CCDC) under deposition number CCDC 2178500. These data can be obtained free of charge from The Cambridge Crystallographic Data Centre via www.ccdc.cam.ac.uk/data_request/cif.

Submitted 19 June 2022
Accepted 17 October 2022
Published 2 December 2022
10.1126/sciadv.add5660